Eur. Phys. J. C 52, 477–485 (2007)
DOI 10.1140/epjc/s10052-007-0383-7

THE EUROPEAN
PHYSICAL JOURNAL C

Special Article – Young Scientists Paper

Search for the lepton flavour-violating decay $\mu \to e\gamma$

The MEG experiment probes GUT scale physics with MeV particles

Y. Hisamatsu[a]

Department of Physics, Graduate School of Science, The University of Tokyo, 7-3-1 Hongo, Bunkyo-ku, Tokyo, Japan

Received: 25 June 2007 /

Abstract. I introduce the upcoming MEG experiment, which will search for the rare decay $\mu \to e\gamma$ down to the branching ratio of 10^{-13}. In order to suppress the background and achieve this unprecedented sensitivity, a great deal of thought went into designing this experiment. Here, I describe the essential components of this experiment, the beam line, the positron spectrometer, and the liquid xenon γ-ray detector.

PACS. 29.40.Gx; 29.40.Mc

1 Introduction

Studies on flavour-violating processes have provided us with a detailed picture of the flavour structure of quarks and leptons. The flavour mixing among quarks arises when quarks couple to the Higgs field by Yukawa interactions. This is described by the off-diagonal terms in the Cabibbo–Kobayashi–Maskawa matrix within the framework of the Standard Model (SM), and has been studied intensively in many experiments. The mass matrix of charged leptons, on the other hand, is fully diagonal because of the absence of right-handed neutrinos. Therefore, flavour mixing in the lepton sector is explicitly forbidden in the SM.

The recent discovery of neutrino mixing has, however, shed light on the physics beyond the SM. Neutrino masses and mixing can be explained by introducing the Yukawa coupling of right-handed neutrinos, and the natural explanation of small neutrino masses is provided by the seesaw mechanism which predicts that neutrinos are Majorana particles. This extended-SM scenario implies the existence of flavour violation among charged leptons, and one such process, $\mu \to e\gamma$, which is the focus of the MEG experiment, is shown in its SM-form in Fig. 1a. However, the predicted rate of flavour mixing for charged leptons is still infinitesimal. The branching ratio of $\mu \to e\gamma$ is predicted to be $\mathrm{Br}(\mu \to e\gamma) \leq \mathrm{O}(10^{-40})$ [1].

In the SUSY-GUT framework [2–4], quarks and leptons have superpartners and are unified into larger multiplets. When such theories are brought down to the SUSY-breaking scale, the Yukawa interaction induces the radiative corrections, which result in the off-diagonal term in the slepton mass matrix and an observable rate of flavour mixing for charged leptons. Taking again $\mu \to e\gamma$, which so far has never been observed, Fig. 1b shows one of the possible processes as predicted by SUSY–GUT scenarios. Such models, together with the neutrino parameters obtained from the observation of neutrino oscillations, predict the rate of $\mu \to e\gamma$ to be around $10^{-11} - 10^{-14}$.

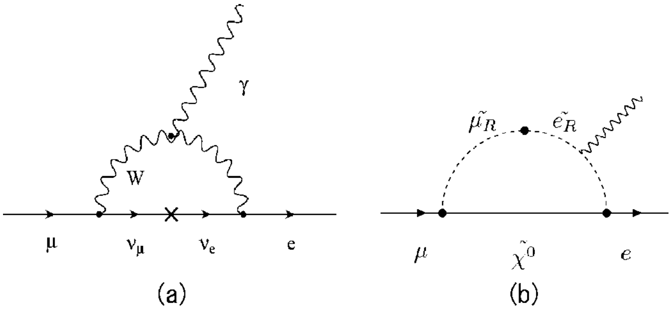

Fig. 1. Possible processes of $\mu \to e\gamma$ in (**a**) the SM and (**b**) SUSY–GUT

In the following sections I introduce the upcoming MEG experiment [5, 6], a dedicated search for the $\mu \to e\gamma$ decay.

2 The MEG experiment

The MEG experiment plans to search for $\mu \to e\gamma$ down to a branching ratio of 10^{-13}, two orders of magnitude below the present limit of 1.2×10^{-11} [7]. Therefore, with the above-mentioned current predictions, MEG has a real chance for probing GUT-scale physics.

In order to achieve this, however, we need a large number of low energy muons and a precision detector. The MEG experiment will measure the decays of up to 10^8 stopped muons

---

[a] e-mail: pekochan@icepp.s.u-tokyo.ac.jp

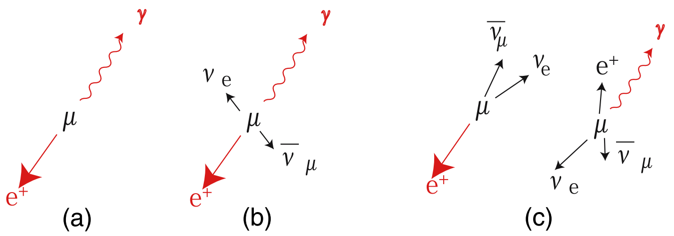

Fig. 2. Kinematics of (1) $\mu \to e\gamma$, (2) radiative muon decay and (3) e.g. accidental overlap event between e^+ from Michel decay and a γ-ray from radiative decay

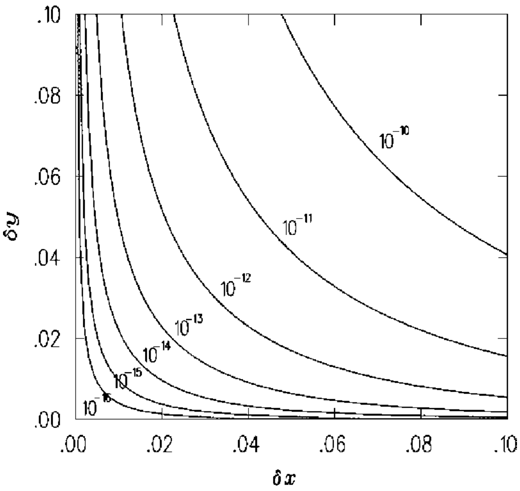

Fig. 3. Effective branching ratio of the physics background from muon radiative decay as a function of the e^+ energy resolution δx and photon energy resolution δy. δx and δy are defined as the half-widths of $\mu \to e\gamma$ signal region for $x = 2\,E_e/m_\mu$ and $y = 2\,E_\gamma/m_\mu$ [8]

per second with unprecedented sensitivity. The resolution of the detectors will be introduced in Sect. 4.

The kinematics of $\mu \to e\gamma$ is quite simple (Fig. 2); a two-body decay with a positron and a γ-ray emitted back-to-back, at the same momentum (52.8 MeV/c), and coincident in time. Concerning the background of the $\mu \to e\gamma$ decay, there are two major sources; 1) physics background from radiative muon decay $\mu^+ \to e^+ \upsilon_e \overline{\upsilon}_\mu \gamma$, and 2) accidental background, the coincidence between a positron from Michel decay ($\mu^+ \to e^+ \upsilon_e \overline{\upsilon}_\mu$) and a γ-ray coming from other sources (Fig. 2). Taking into account our detector performance, the accidental background is the more serious of the two backgrounds since the phase space of the radiative decay is strongly limited when the positron and photon energies are almost half of the muon mass, thus mimicking a $\mu \to e\gamma$ decay as shown in Fig. 3 for good energy resolutions.

The key to suppressing such accidental background is a good quality muon beam and precision detectors with unprecedented sensitivity. A great deal of very careful consideration went into designing this challenging experiment; the beam line provides a high-rate continuous muon beam in order to reduce accidental background. A tremendous effort went into making the drift chambers out of low mass material so that they could measure low energy positrons precisely. Great care was taken in selecting the scintillating material for the timing counter to achieve the best possible timing resolution, 100 psec (FWHM). An innovative gamma detector based on liquid xenon was developed for the precise measurement of position, energy and timing of the γ-ray.

In the following sections, these essential components of the experiment are described.

3 Beam line

3.1 π E5 beam line at the Paul Scherrer Institut

The MEG experiment will be conducted at the π E5 beam line at the Paul Scherrer Institut (PSI) Switzerland, where the world's most intense DC muon beam is available.

PSI has a long tradition of pion and muon physics with its isochronous ring cyclotron capable of accelerating protons to 590 MeV at a current close to 2 mA. The extracted 1.1 MW beam with 50 MHz time structure is delivered to two graphite target stations which serve several secondary beam lines.

The π E5 beam line extracts so-called "surface muons", 100% polarized and initially monoenergetically produced muons of 29.79 MeV/c from stopped pion decay, close to the surface of the production target [9]. These are transmitted in a narrow momentum band ($\delta p/p \sim 8\%$ FWHM), centered around 28 MeV/c, and originate from muons born at somewhat greater depths in the target. Due to the muon lifetime and the radio-frequency structure of the proton beam, a DC muon beam is produced, which has distinct advantages for a coincidence experiment such as $\mu \to e\gamma$. For example, the instantaneous rate is lower than a pulsed beam and offers less accidental background, which increases quadratically with beam rate. The narrow momentum band also makes it easier to stop the particles in a very thin target, which also helps to minimise the production of background particles which can enter the detector.

3.2 MEG beam transport system

The purpose of the MEG beam transport system is 4-fold: (1) to transmit the high intensity surface muon beam with minimal losses, (2) stop the maximum number of muons in the thinnest and smallest possible target at the centre of the MEG detector, (3) produce a source of maximally depolarised muons at the target, (4) minimise the transmission of unwanted beam positrons and background.

In order to achieve these aims, a beam transport system comprising two sets of quadrupole magnets arranged as "Triplets" is used (see Fig. 4). The first triplet enables the optimal injection of the beam into the crossed field separator (WIEN-filter), which runs at 200 kV. The second triplet focuses the well-separated (7.5σ) muon and beam-positron spots onto a collimator system placed between it and the beam transport solenoid BTS, allowing the transmission of a pure muon beam from the initial e/μ ratio of 8 : 1.

The BTS, a 2.8 m long, 38 cm diameter warm-bore superconducting solenoid, runs at a maximum magnetic

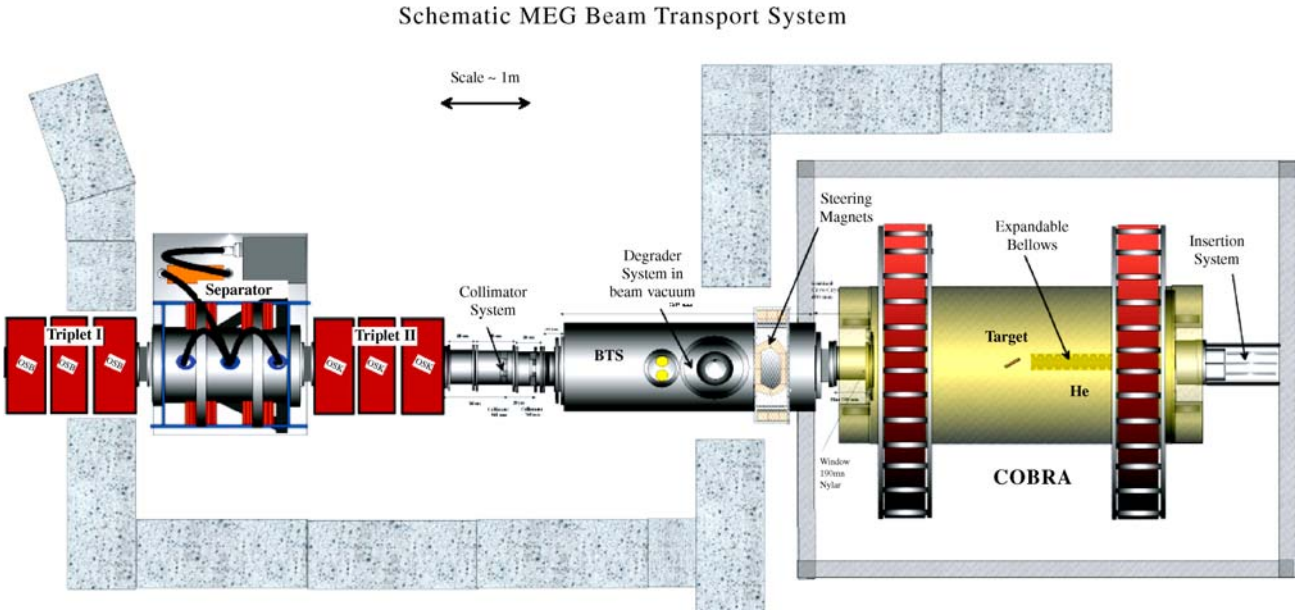

Fig. 4. Schematic of the π E5 MEG beam line at PSI. Muons enter from the left through a quadrupole triplet magnet, and then pass through a Wien filter, and are focused by a second quadrupole triplet onto a collimator, which transmits muons to the BTS and degrader system before being focused onto a target at the centre of the MEG detector (COBRA)

field of 0.5 T. A CH_2 degrader system placed at the central focus of the BTS reduces the momentum of the muons, which must traverse 1.5 m of He-gas to reach the centre of the COBRA spectrometer, where they are stopped in a 150 μm thick CH_2 target that is inclined at about 20° relative to the incoming beam.

The MEG beam transport system has so far been able to deliver a beam of 1.1×10^8 μ^+/s at 1.8 mA proton beam current, with a beam spot size of $\sigma \sim 11$ mm to the target.

4 The MEG detector

The MEG detector consists of a positron spectrometer called COBRA (constant-bending-radius) and a liquid xenon gamma detector. The spectrometer is comprised of 3 main components: 1) the COBRA magnet, which is a special gradient-field superconducting magnet, as described in Sect. 4.1.1; 2) a set of low-mass radial drift chambers as tracking devices, detailed in Sect. 4.1.2; and lastly, 3) a set of fast double-layered scintillation timing-counter arrays, placed at either end of COBRA to give both timing and trigger information. These are described in Sect. 4.1.3. The γ-ray, originating from the target, traverses the thin walls of COBRA and is converted into an electromagnetic shower in the liquid-xenon gamma detector, described in Sect. 4.2.

4.1 COBRA positron spectrometer

4.1.1 COBRA magnet

The superconducting COBRA magnet [10] forms a special gradient field (1.27 T at the centre to 0.49 T at both ends), as shown in Fig. 6. The magnet consists of five coils of three different radii, with the field gradient produced by this step-structure in the coil layout as well as by the winding density of the conductor in each coil. A high-strength aluminum-stabilised conductor was developed for this magnet to minimise the thickness of the support structure. The conductor itself, a copper matrix with a NbTi multi-filamentary core, is embedded in an aluminium stabiliser mechanically reinforced by "micro-alloying" and "cold work hardening" technologies [11, 12]. The aluminum stabiliser can be reinforced by adding a small amount of metal, such as nickel, magnesium or copper, while keeping electrical resistivity as low as possible; in this case, 5000 ppm of nickel was added. The total thickness of the central part of the magnet, where the γ-ray traverses, is in this way reduced down to 0.193 X_0.

The magnet is equipped with a pair of resistive compensation coils in order to cancel the stray field from the superconducting magnet in the vicinity of the LXe gamma detector. Any external magnetic field would deteriorate the performance of the photomultiplier tubes used in the LXe gamma detector. A residual field of less than 50 Gauss is achieved over the whole region of the LXe gamma detector.

In the gradient field, positrons with the same absolute momenta follow trajectories with a constant projected bending radius, independent of their emission angle as shown in Fig. 7a. This allows only the higher momentum positrons from the high-rate Michel decays to enter the drift chambers, thus helping to prevent accidental overlap events, which cause unwanted dead-time. This also helps to sweep away positrons quickly and prevents them from making many turns inside the tracking volume, as shown in Fig. 7b.

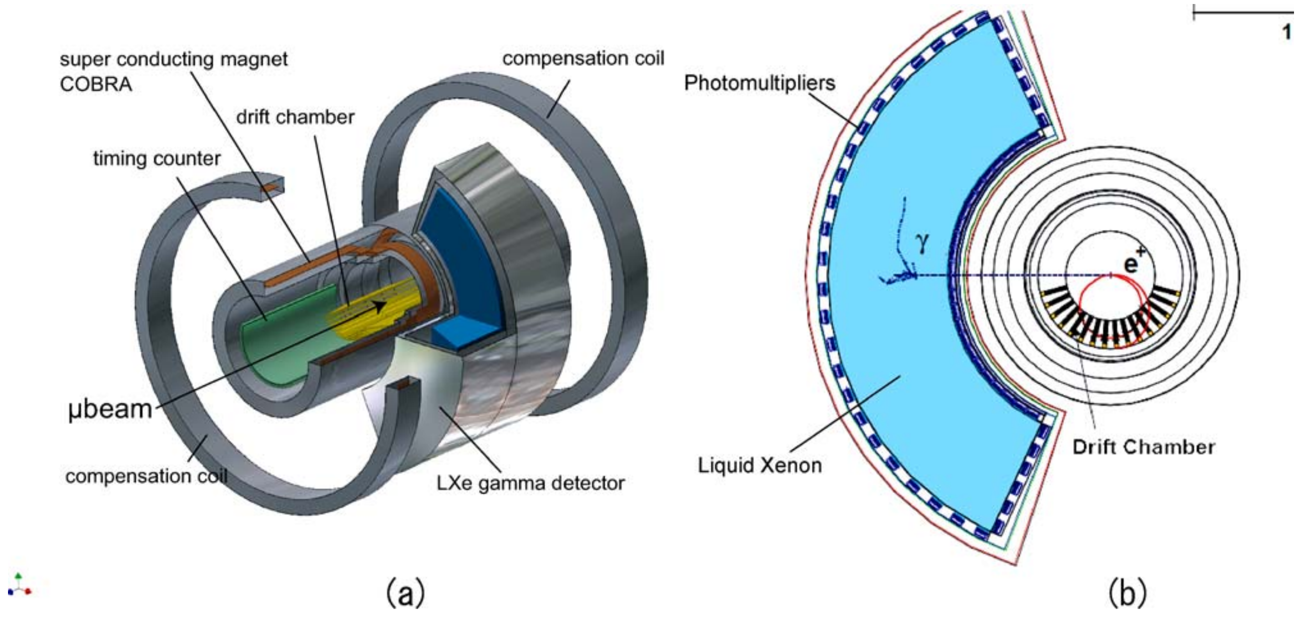

Fig. 5. (**a**) Schematic view of the MEG detector, and (**b**) cross-sectional view of the MEG detector

4.1.2 Drift chamber

The MEG drift chamber system [13] is placed radially around the target region, as indicated by the yellow trapezoid in Fig. 5.

It is composed of 16 modules, each with 2 layers of anode planes of nine drift cells each. The drift-cell of each layer is characterised by a central anode wire and two potential wires on either side, spaced 9 mm apart. Orthogonal to and 3.5 mm on either side of the wire plane are two Vernier Pad cathode planes. The two layers are staggered by a half-cell to resolve the left–right ambiguity. The sense wires are read out at both ends, as shown in Fig. 8. The ratio of charges measured at both ends provides the approximate position of the particle along the wire (z-coordinate) with $\sigma \sim 1$ cm resolution. From this information, the correct cycle of the repeating Vernier pad pattern is chosen, and a more precise z-coordinate is determined from the induced charge on the Vernier pads of the two associated parallel cathode planes on either side of the wire. The Vernier pattern of each cathode is shifted by 1/4 of a period to obtain a homogeneous resolution along the wire. For the z-direction, $\sigma_z = 300$–$500\,\mu$m, and by meas-

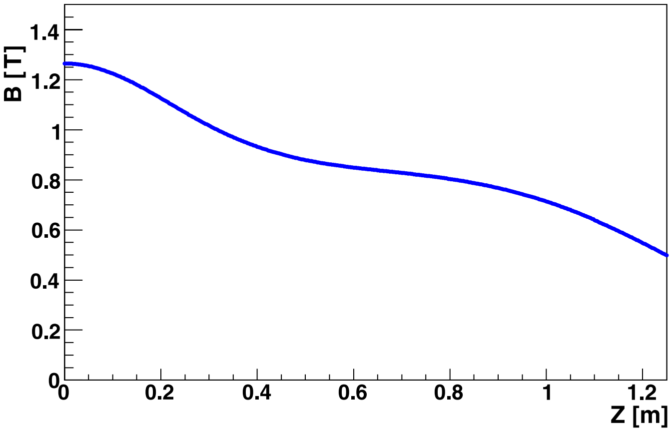

Fig. 6. Measured magnetic field of the COBRA magnet along the beam axis

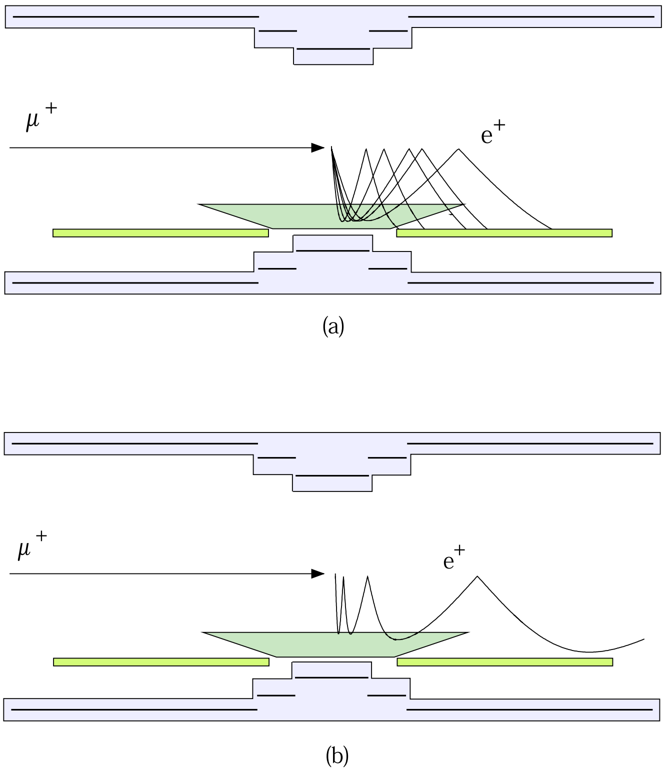

Fig. 7. Principle of the COBRA spectrometer; advantages of a gradient magnetic field

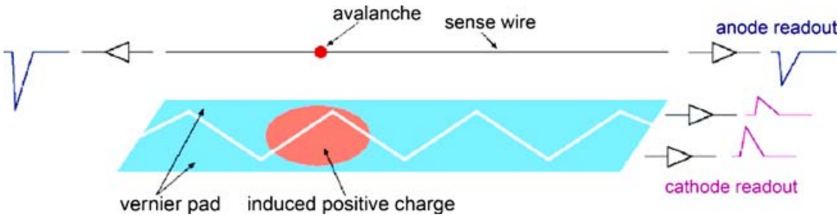

Fig. 8. Read-out scheme of the drift chamber. The sense wire is read out from both ends for a rough position reconstruction. Vernier pads are used for a more precise reconstruction

Fig. 9. Anode frame with wires (*front*); cathode frame with the Vernier foil (*middle*); completed drift chamber (*back*)

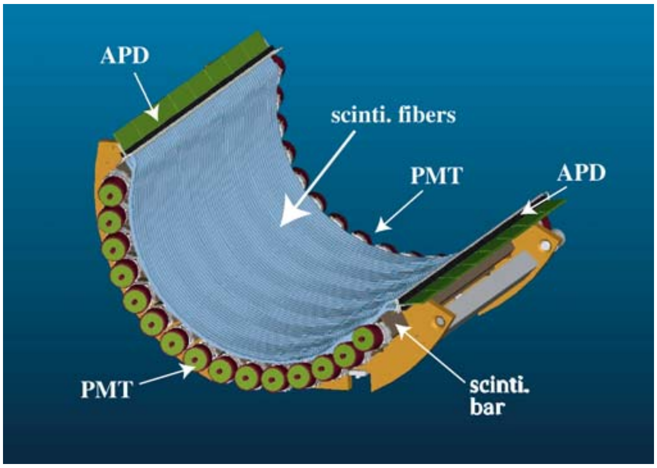

Fig. 10. Schematic view of a timing counter array. PMTs are connected to both ends of the scintillator bar. Scintillation fibres cover the scintillator bars and are read out by APDs

uring the drift time for the distance of the track to the wire, $\sigma_r = 100$–$200\,\mu$m are resolutions that have been obtained from tests with a prototype chamber. This good position resolution of the drift chamber is crucial for the precise determination of the opening angle between the positron and the gamma as well as for determining the positron momentum.

The MEG drift chambers are designed as a low-mass chamber system in order to minimise multiple scattering and γ-ray generation inside the chamber. The chamber gas is a helium-based mixture ($\mathrm{He:C_2H_6} = 1:1$). The chamber walls are made of a thin foil ($12.5\,\mu$m thick polyimide with 2500 Å aluminium deposition), and the frames of the chamber are made of carbon-fibre. Moreover, material could further be reduced by making the chamber frames in a truncated "V-shaped" structure, open on the target side (Fig. 9). Thanks to these exhaustive efforts, the overall material along the positron track is reduced to 1.5×10^{-3} of a radiation length.

The drift chambers successfully experienced their first engineering run at the π E5 beam line of PSI in December 2006, where they were exposed to Michel positrons generated by $10^7 \sim 10^8$ muons/s. Currently, the data from the chamber is being analysed with respect to the chamber calibration and resolutions.

4.1.3 Timing counter

After leaving the drift chambers, positrons enter a set of plastic scintillation counters and scintillating fibre bundles called timing counters, which are placed axially on either side of the drift chambers [14]. The counters are intended to provide the precise timing of the positrons with 100 ps FWHM resolution, whereas the fibre bundles are used for the first-level trigger to determine the positron direction with respect to the γ-ray. The schematic view of a timing counter array is shown in Fig. 10.

The counters are made up of 15 plastic scintillator bars whose dimensions are $4 \times 4 \times 90$ cm, and their output is read by photomultipliers connected at both ends. The bars are made of Saint-Gobain Crystals – BC404 scintillator with a fast rise time of 700 ps. They are rotated by 20° with respect to the radial axis, as shown in Fig. 11a, in order to obtain a uniform track length for all positrons, which helps to make the pulse height distribution narrow. The PMTs are directly attached to each bar without using light guides to avoid a timing spread. Since one of the PMTs is placed close to the centre of the COBRA magnet, where the magnetic field is 1 T, fine-mesh PMTs of type R5924 from Hamamatsu Photonics are adopted. The PMTs are also tilted by $\sim 20°$ with respect to the magnetic field in order to create a "zero-field" environment inside them, which helps to reduce the loss of their gain (Fig. 11).

The timing resolution of the counters was measured with an electron beam at the Test Beam Facility in the Laboratori Nazionali di Frascati. The counters were irradiated with 25–550 MeV e^+ and 25–800 MeV e^- with a spot-size of $\sigma_z = 5$ mm. Here, z is the coordinate along the counters. The timing resolution was measured at 6 points along the bar at intervals of 10 cm, and the excellent resolution of ~ 100 ps FWHM was achieved at all measured points.

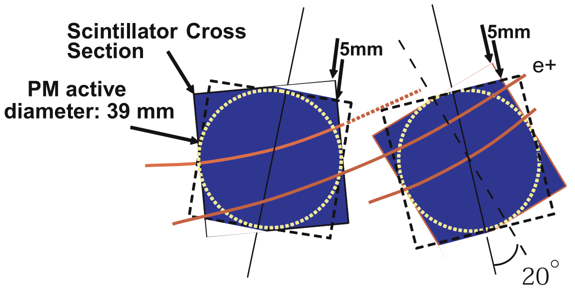

(a) Sectional View

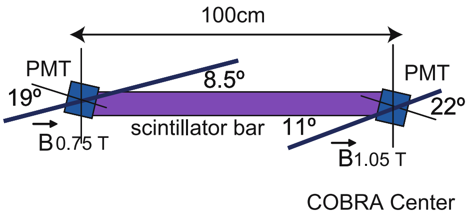

(b) Longitudinal View

Fig. 11. (**a**) Cross-sectional view of a TC bar. The scintillator bar is slightly tilted to give a uniform track length of e^+. (**b**) Longitudinal view of a TC bar. The PMT is attached to the scintillator bar and is also slightly rotated

4.2 Liquid xenon gamma ray detector

An innovative liquid xenon (LXe) scintillation detector was devised for this experiment in order to make very precise measurements of the energy, position and timing of the γ-rays. The detector consists of 900 litres of LXe as a scintillator and 846 photomultipliers (PMTs) for the collection of scintillation light. LXe is viewed from all sides by PMTs which are directly immersed in LXe (Fig. 5). This characteristic design, which is similar to that of the Kamiokande detector, has distinct advantages: a high light yield from the scintillation light of LXe, fast scintillation signals and a homogeneous, non-segmented medium viewed via direct light, which gives a very good uniformity and allows a large active volume.

The performance of such a detector depends largely on the amount of scintillation light collected by the PMTs, but also on the transparency of the medium as well as a homogeneous PMT coverage. The energy of a γ-ray is determined by the total amount of scintillation light, and the incident position is calculated from the distribution of scintillation light on the detector walls. The arrival time of scintillation light at each PMT determines the timing of the γ-ray. This led us to conduct an intensive study on the optical properties of LXe and the development of PMTs to improve the collection of scintillation light, as described in Sect. 4.2.1 and Sect. 4.2.3.

Some of the novelties of this detector include how its special C-shaped form helps to minimise the quantity of LXe needed, and that the PMTs are operated inside the LXe, which is challenging from the point of view of both γ-ray detectors and cryogenics. The cryogenic detector operation was also optimised by the introduction of a pulse-tube refrigerator, suitable for LXe, which significantly reduces the vibrational noise at the cold-head. This is introduced in Sect. 4.2.2.

4.2.1 Liquid xenon as scintillator

LXe has a high light yield and a fast decay time, which are advantageous for precise energy measurements and the identification of pile-up γ-rays. The optical properties of LXe are listed in Table 1. The conversion from energy to scintillation photons is done by the formation of an excited state of Xe; $\mathrm{Xe}_2^* \to 2\mathrm{Xe} + h\upsilon$. Here, $h\upsilon$ is a vacuum-ultraviolet photon, which is not absorbed by the xenon itself since the inverse reaction, $2\mathrm{Xe} + h\upsilon \to \mathrm{Xe}_2^*$, does not occur. In principle, LXe is transparent to its scintillation light. However, impurities like water (even at the ppm-level) or oxygen (to a lesser extent) absorb scintillation light considerably, which leads to a deterioration of the detector performance. Hence, the evaluation of the LXe absorption length [15] is essential for understanding the LXe detector response. This is briefly described in Sect. 4.2.4.

Our group worked intensively to develop a purification system for LXe [16]. The initial efforts were focused on gas-phase purification, from which it was found that the main absorption comes from water [17]. This led to the current liquid-phase purification system, dedicated to the removal of water. This system consists of molecular sieves (MS13A) and a cryogenic centrifugal pump from BarBer-Nichols Inc., and it aims at removing water, the main impurity responsible for the absorption of scintillation light in our detector. Its performance was tested with 100 litres of LXe, and the impurity concentration was successfully reduced from 250 ppb to 50 ppb within 5 hours. With this purification system, LXe is free from the problem of the degradation of its optical properties during the detector operation. This is one great advantage that the LXe detector has over other crystal detectors, which are difficult to purify during their operation.

4.2.2 Cryogenics for liquid xenon

One of the main requirements of the LXe Cryogenic System is that of temperature stability, which is necessary to ensure the stable operation of the PMTs in the cryo-fluid. This was the reason for choosing a refrigeration system over conventional cooling. Furthermore, by using a pulse-tube refrigerator [19], which has no moving parts in the cold-head, a minimum of intervention is needed inside the

Table 1. Properties of LXe

Emission peak	178 nm
Spectral width	14 nm
Refractive index	1.62 ± 0.05 [18]
Decay time (recombination)	45 ns
Decay time (fast components)	4.2 ns
Decay time (slow components)	22 ns

system and no vibrational noise is transmitted to the detector. To allow for efficient liquefaction, retention and re-condensation of the LXe in our detector, we employed a compact system (developed by KEK and the Iwatani Gas Co.) with a heat capacity of 200 W, which was sufficient for our needs. During the operation of the prototype detector, a pressure and temperature stability of ±0.001 MPa and ±0.1 K, respectively, were maintained.

4.2.3 Photomultiplier for liquid xenon

In order to view the 178 nm scintillation light, the PMTs are directly immersed in 167 K LXe, a severe environment for their operation. This environment poses constraints on the types of materials that can be used, as is apparent from the perspectives of contamination and thermal shock. Heat dissipation was carefully considered during the design of the base-circuit of the PMTs. Finally, the fact that the PMT housing would have to withstand pressures of up to 3 bar also required careful R&D. A photocathode sensitive to the VUV range was required, with added difficulty coming from the high electrical resistivity of the photocathode at low temperatures, which decreases quantum efficiency and degrades photoelectron emission in high-rate counting environments.

To overcome these difficulties, a new type of PMT (Fig. 12) was developed together with Hamamatsu Photonics Inc. It has a special low surface resistivity K−Cs−Sb photocathode, made by forming an aluminium strip pattern on the silica window first, and then evaporating the photocathode material. In order to make a compact type of device, a metal channel dynode structure that could function in magnetic fields up to 50 Gauss was used.

The characteristics of the base circuit (shown in Fig. 13) feature a high resistance voltage divider to minimise heat dissipation and Zener diodes placed between the last two dynodes as a voltage regulator to stabilise the PMT gain in high-rate environments. Noise filtering resistors are also placed in series with the diodes that filter at low temperature. The PMT output linearity has been confirmed above a dynode current of 4 μA, which is sufficient for our operational conditions.

So far, over 1000 PMTs have been manufactured by Hamamatsu Photonics Inc. in Japan, and tested for performance prior to their installation in the LXe γ-ray detector. The tests were conducted using a large prototype detector, which will be described in Sect. 4.2.4, and a PMT test facility at INFN Pisa [20]. The quantum efficiency (QE) was measured to be 16% on average, and their good stability in high-rate counting environments was confirmed [21].

Fig. 12. Photomultiplier for the MEG LXe detector

4.2.4 Monitoring and calibration of the detector

The good performance of the LXe detector is assured by stability monitoring and precise calibration. The stability is monitored using special α-sources mounted in the detector. Several point-like ^{241}Am α-sources (200–300 Bq each) are deposited on a 100 μm diameter wire, several of which are stretched inside the detector [22]. α-particles deposit a constant energy in the liquid, resulting in the emission of a constant amount of scintillation light from all points, as if the sources were floating in the liquid. The PMT long-term stability is monitored using this method. In addition, the PMT response linearity can be investigated by observing α-source events under different conditions of beam intensity.

The transparency of the liquid is another important parameter to be monitored. The scintillation light in the liquid suffers from Rayleigh scattering and absorption. The

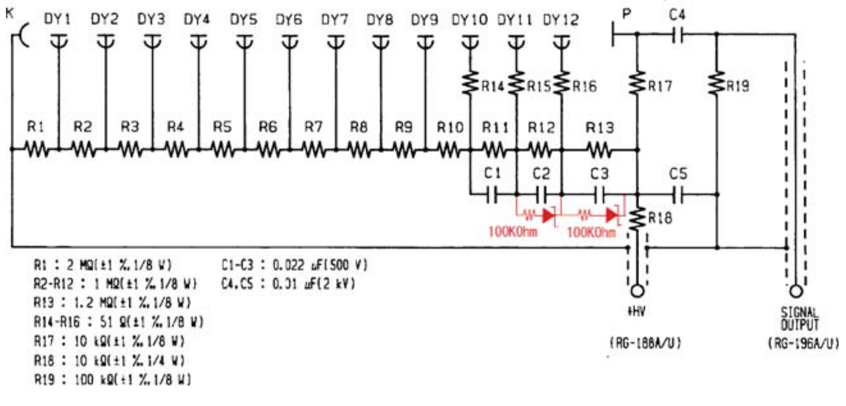

Fig. 13. PMT Base circuit: a Zener diode is placed between the last two dynodes, as indicated in *red*

Rayleigh scattering length is determined by the electron density of the liquid and is considered to be constant, while the absorption length can differ depending on impurity levels. Point-like α-sources are utilized to monitor this as well. The amount of scintillation light observed by each PMT is plotted as a function of the PMT to α-source distance and compared to a simulation, taking into account the effect of detector geometry and Rayleigh scattering. The resulting plot is then fitted with an exponential function to evaluate the absorption length, which in the simulation is assumed to be infinite. This method has been tested in the detector development phase using a prototype, as explained in [22].

Calibration of the detector is performed in several steps. First, the PMT gains are adjusted to within 3% of each other by using blue LEDs mounted in the detector. The gain of each PMT is evaluated using photo–electron statistics, as described in [15], and then is periodically measured during detector operation. The quantum efficiency (QE) of the PMTs is evaluated by comparing Monte Carlo (MC) simulation data with α-source data taken in cold (< 170 K) gaseous xenon. Gaseous xenon is used since it contains fewer impurities, so that the QE can be obtained from the PMT outputs without having to take into account the absorption. All of these calibration data are stored in a database and used in offline analysis.

The detector is both monitored and calibrated periodically with γ-rays of various energies. Four methods are employed, over a wide energy range: 1) 4.43 MeV γ-rays produced by an Am/Be radioactive source, 2) 9 MeV γ-rays produced by neutron capture on nickel, from a polyethylene-moderated Californium neutron source, 3) 17.6 MeV γ-rays produced by the $^7\mathrm{Li}(p,\gamma)^8\mathrm{Be}$ resonance excitation in a LiF target, bombarded by a 500 keV proton beam from a Cockcroft–Walton accelerator, 4) 55 MeV, 83 MeV and 129 MeV γ-rays obtained from dedicated runs with a negative pion beam, stopped in a liquid hydrogen target placed at the centre of our detector. The lower two energies originate from the pion charge-exchange reaction $\pi^- p \to \pi^0 n$, selecting back-to-back γs from π^0-decay, while the higher energy γ-ray comes from the radiative capture reaction $\pi^- p \to \gamma n$.

4.2.5 Performance evaluation

We constructed a prototype detector to evaluate its performance and to gain experience in operating such a detector and handling xenon liquefaction and purification. The active volume of the prototype is $372 \times 372 \times 496\,\mathrm{mm}^3$ (69 liters) and it is surrounded by 228 PMTs assembled in a rectangular formation in a cryostat, as shown in Fig. 14. Performance evaluation was carried out by using γ-rays from π^0 decay in the charge-exchange reaction and from radiative capture. The PMT gain and QE calibrations were conducted as described above. The xenon was purified before starting data acquisition by using the method described in [17] to obtain a sufficiently long (~ 3 m) absorption length relative to the detector size. An array of NaI crystals with a ~ 5 cm diameter collimator for tagging γs was located on the opposite side of the LXe detector.

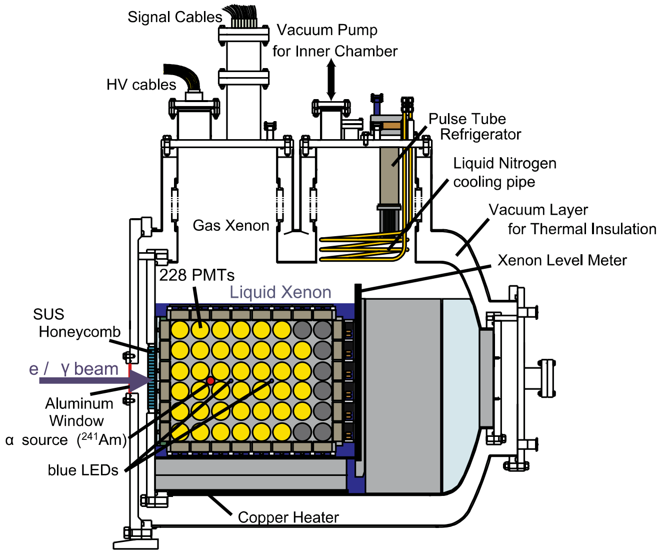

Fig. 14. Schematic view of the large prototype LXe detector

The γ-ray in the LXe detector is reconstructed by using the charge information collected by the PMTs. Its energy is reconstructed by summing all of the PMT outputs after calibration. In reconstructing the position and timing of the γ-ray interaction, we select only those PMTs that observed a relatively large charge, on the entrance face, in order not to suffer from shower shape fluctuations. The γ-ray interaction position is reconstructed by taking the weighted mean of PMT locations according to the observed charge as expressed below:

$$X = \frac{\sum_{\mathrm{selected}} q_i X_i}{\sum_{\mathrm{selected}} q_i}\,. \tag{1}$$

The depth of the interaction point is evaluated by using the spread of the light distribution on the entrance face. If a γ-ray deposits energy near the entrance face, the entrance face receives scintillation light with a small spread, while if it occurs deep in the detector, the spread becomes broader, as shown in Fig. 15.

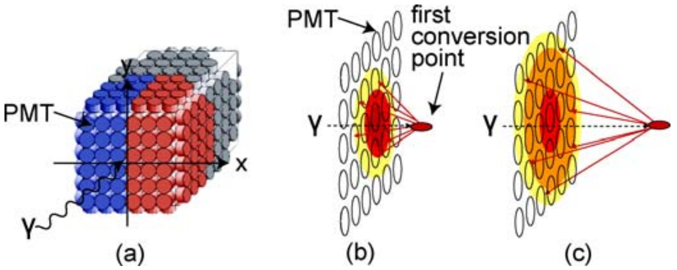

Fig. 15. (**a**) γ-ray impinging at the centre of the large prototype "front face". The "depth" is the distance along the z-axis. (**b**) Light distribution on front face with a shallow conversion point. (c) Light distribution on front face with a deep conversion point

Performance evaluation tests were carried out twice at PSI with different sets of PMTs, resulting in an energy resolution of 4.8% (FWHM), a position resolution of 4.9 mm (FWHM) and a timing resolution of 45 ps (sigma) for 55 MeV γ-rays [21]. This performance has convinced us of the future success of the LXe detector. Construction of the final LXe detector is in progress now and its engineering run will be performed in 2007.

5 Summary

Lepton flavour violation is a clear sign of physics beyond the Standard Model. The upcoming $\mu \to e\gamma$ experiment, MEG, is very attractive in the sense that we can probe GUT-scale physics by measuring MeV-scale particles. However, this requires the careful design and operation of novel detectors. The MEG is designed to search for the flavour violating decay of muons with an unprecedented sensitivity, 10^{-13}. For the start of the physics run in 2007, we are intensively preparing the beam line, the positron spectrometer and the LXe γ-ray detector. The MEG beam line has succeeded in delivering more than 10^8 muons/s to the centre of the MEG detector. The positron spectrometer has recently measured its first high-rate muon decays in the special gradient magnetic field created by COBRA. The LXe γ-ray detector will measure the energy, incident position, and timing of incoming γ-rays using newly developed cryogenics and photomultipliers. The prototype detector has confirmed the feasibility of obtaining the required resolutions with the final detector. After years of developing our novel detectors, we are now getting ready to probe GUT-scale physics.

Acknowledgements. I would like to thank the International School of Subnuclear Physics (ISSP) Committee of the Ettore Majorana Foundation and the director of this school, Prof. A. Zichichi and Prof. G. 'tHooft for giving me the great opportunity to broaden my view of physics. So many wonderful lectures, from the quark–gluon plasma world to the landscape of string theory vacua, stimulated and exited me. I also appreciate the great encouragement I received from the lecturers and scientists of this school, and this great opportunity to submit a paper as a young scientist.

I would like to express my deep gratitude to Prof. M. Koshiba, Prof. S. Komamiya, and Prof. T. Mori, who sent me to ISSP, thus giving me the opportunity to attend wonderful lectures and stimulating discussions with great scientists.

I would also like to send many thanks to my MEG colleagues, especially, Dr. J. Egger, Dr. P.-R. Kettle, Dr. S. Mihara, Prof. T. Mori and Dr. W. Ootani, who gave me much advice on this paper. Many thanks also go to my two senior colleagues, H. Nishiguchi and R. Sawada. Our discussions on the drift chamber and the calorimetry of the LXe detector taught me many things.

Finally, I would like to express my appreciation to Prof. Luisa Cifarelli and Dr. Silvia Arcelli of the University of Bologna for their great encouragement and patience with the writing of this article.

This work was supported by a Japan MEXT Grant-in-Aid for Scientific Research on Priority Areas 441.

References

1. T.P. Cheng, L.F. Li, Phys. Rev. Lett. **45**, 1908 (1980)
2. J. Hisano, D. Nomura, Phys. Rev. D **59**, 116 005 (1999)
3. L.J. Hall, V.A. Kostelechy, S. Raby, Nucl. Phys. B **267**, 415 (1986)
4. F. Borzumati, A. Masiero, Phys. Rev. Lett. **57**, 961 (1986)
5. T. Mori et al., Research Proposal to Paul Scherrer Institut **R-99-5** (1999)
6. A. Baldini et al., Research Proposal to INFN, (2002)
7. M.L. Brooks et al., Phys. Rev. Lett. **83**, 1521 (1999)
8. Y. Kuno, Y. Okada, Phys. Rev. Lett. **77**, 434 (1996)
9. A.E. Pifer, T. Bowen, K.R. Kendall, Nucl. Instrum. Methods **135**, 39 (1976)
10. W. Ootani et al., IEEE Trans. Appl. Supercond. **14**, 568 (2005)
11. A. Yamamoto, Y. Makida, Y. Doi, T. Kondo, K. Wada, S. Meguro, Nucl. Phys. B **78**, 565 (1999)
12. A. Yamamoto, Y. Makida et al., IEEE Trans. Appl. Supercond. **12**, 438 (2002)
13. H. Nishiguchi, Nuc. Phys. B (2006)
14. S. Dssoniu, PhD thesis (University of Genova, 2006)
15. A. Baldini et al., Nucl. Instrum. Methods A **545**, 753 (2005)
16. S. Mihara et al., Cryogenics **46**, 688 (2006)
17. S. Mihara et al., Cryogenics **44**, 223 (2004)
18. private communication with S. Nakamura from Yokohama National Univ. and with T. Haruyama from KEK
19. T. Haruyama et al., AIP Conf. Proc. **823**, 1695 (2006)
20. A. Baldini et al., Nucl. Instrum. Methods A **566**, 294 (2006)
21. T. Iwamoto, Nucl. Phys. B (2006)
22. A. Baldini et al., Nucl. Instrum. Methods A **565**, 589 (2006)